Available online at www.sciencedirect.com
SCIENCE DIRECT®
International Journal of Heat and Fluid Flow 26 (2005) 755–770
International Journal of HEAT AND FLUID FLOW
www.elsevier.com/locate/ijhff

Numerical simulations of underexpanded supersonic jet and free shear layer using WENO schemes

T.S. Cheng *, K.S. Lee

Institute of Aeronautics and Astronautics, Chung Hua University, 707, Sec. 2, Wufu Road, Tungshiang, Hsinchu, 300, Taiwan, ROC

Received 8 April 2004; accepted 25 January 2005
Available online 25 March 2005

Abstract

Numerical simulations of the flowfield structures and properties of underexpanded supersonic jet and planar shear layer are performed by solving the time-dependent, compressible Euler equations. The numerical code uses the high-order weighted essentially non-oscillatory (WENO) finite difference schemes with the fifth-order-accurate for spatial discretization and the fourth-order-accurate Runge–Kutta scheme for time integration. The present predictions are compared with the available experimental data and other numerical results using different numerical schemes. Good agreements between the predicted and experimental data are achieved for both cases. The results show that the near-field region of the jet and shear layer is influenced by compressibility, which reduces turbulent mixing rates and suppresses vortex roll-up and pairings at high-convective Mach number. Analyses of sound pressure level of the jet indicate that the broadband shock noise is generated from the shock cells and radiates in the direction of 40°–50° to the jet axis. Various forcing frequencies are applied at the inflow boundary to demonstrate mixing enhancement and shock cell destruction for the underexpanded jet. The computation of an underexpanded free shear layer indicates that the numerical turbulence model inherent with WENO algorithm can satisfactorily predict turbulence properties at a convective Mach number of 0.64 even without including subgrid-scale turbulence models.

Keywords: Supersonic jet; Free shear layer; WENO schemes; Sound pressure level; Mixing enhancement

1. Introduction

The development of appropriate computer models for supersonic propulsion systems holds the potential for their computer-aid design with lower development costs, higher mixing efficiencies, lower pollutant and noise emissions, and wider fuel specifications. However, to be reliable over a wide range of applications, such models should be based upon a fundamental, quantitative understanding of the complex interaction of turbulent mixing and the structure of the flowfield. Supersonic injection of an imperfectly expanded air jet into still air and supersonic/subsonic free shear layer are two of the simplest flows for investigation. Supersonic imperfectly expanded (underexpanded/overexpanded) free jets and shear layers are important fundamental flows, involving interactions between supersonic shock-wave-containing compressible flow and noise production. These flows also have a variety of engineering applications, e.g., rocket plume signature predictions, gaseous fuel injection systems, breaks and vents in high-pressure systems, aircraft plume/afterbody interaction problems, and scramjet engines. In order to understand these complex shock-wave interaction processes, to predict the experimentally limited flow properties at the shock-containing regions, to visualize flow structures, and to devise techniques for mixing enhancement and noise reduction in supersonic flows, high-accuracy numerical algorithm must be used.

* Corresponding author. Tel.: +886 3 5186489; fax: +886 3 5186521.
E-mail address: tscheng@chu.edu.tw (T.S. Cheng).

0142-727X/$ - see front matter © 2005 Elsevier Inc. All rights reserved.
doi:10.1016/j.ijheatfluidflow.2005.01.006

Notation

a	speed of sound
D	nozzle exit diameter
e	total energy per mass
F, G	flux vectors
f	frequency
L	spatial operator
M	Mach number
M_c	convective Mach number
p	pressure
p_{ref}	reference pressure
p'_{rms}	root mean square pressure fluctuation
S	source term vector
t	time
U_c	convective velocity
U_e	nozzle exit velocity
U_1	upper stream velocity
U_2	lower stream velocity
$\overline{U}$	average inlet velocity
U^*	normalized mean streamwise velocity
u	streamwise (axial) velocity component
v	transverse (radial) velocity component
W	conservative variable vector
x	axial coordinate
y	transverse coordinate
y_0	the location where $u = \overline{U}$
y^*	normalized transverse coordinate, $(y - y_0)/\delta_w$

Greeks

α	maximum eigenvalue
δ_w	vorticity thickness, $(U_1 - U_2)/(\partial u/\partial y)_{\max}$
θ	dimensionless momentum thickness
θ_0	initial momentum thickness
γ	ratio of specific heats
ρ	dimensionless density
σ_u	streamwise turbulence intensity
σ_v	lateral turbulence intensity

Subscripts

e	nozzle exit condition
i, j	axial and radial grid points
rms	root-mean-square fluctuation
ref	reference value
1	upper stream
2	lower stream

Superscripts

n	time step
$+$, $-$	positive and negative fluxes
$\sim$	numerical flux

In the past, a number of experimental investigations have been made on the underexpanded jets to study the shock wave pattern near the jet exit (e.g., Adamson and Nicholls, 1959; Crist et al., 1966; Davidor and Penner, 1971; Addy, 1981; Ewan and Moodie, 1986) and the shock associated noise (Seiner and Norum, 1980). Measurements of the near-field properties of underexpanded jets are relatively limited, due to difficulties caused by varying static pressures, high velocities, and shock waves. In the near-field shock-containing region measurements were generally limited to mean static pressures using probes for flows generated by converging–diverging nozzles, see for instance Seiner and Norum (1979, 1980). Although detailed measurements of mean velocities and concentrations in underexpanded jets have been made using laser Doppler anemometry (LDA), problems of lag biasing of seeding particles to the rapid changes of velocities across shock waves limited their most reliable data to the constant-pressure region of the flow (Ewan and Moodie, 1986; Cheuch et al., 1989). For jet noise reduction studies, various methods have been proposed to improve mixing. Mixing enhancement of high and low speed streams is utilized as a means to improve efficiency of supersonic combustion, reduce aircraft signatures, and control high-speed jet noise. The introduction of streamwise vorticity by prism shaped wedges has been successfully investigated experimentally (Dolling et al., 1990; Samimy et al., 1993; Zaman et al., 1993; Hu et al., 2000). Mixing enhancement was achieved by the production of large-scale streamwise vorticity, which promotes mixing due to an increase in perimeter contact between low and high-speed streams. In these studies the enhanced jet mixing rates were used as a measure of jet noise reduction, although the required acoustic information has not been measured. The experimental works indicate that an alternative technique, such as numerical method, may help to resolve the flow structures and to obtain the flowfield properties in the shock-containing region of the imperfectly expanded flows. In addition, various methods to increase mixing and hence noise reduction can be investigated using numerical simulations.

Theoretically, a number of approximate methods have been proposed to estimate the flow structure of the underexpanded jets (Ewan and Moodie, 1986; Birch et al., 1984; Tam et al., 1985; Gore et al., 1986). However, most analyses have been confined to streamwise positions far from the jet exit, due to difficulties of exact treatment of the near-field shock-containing region. There have been several numerical simulations to analyze underexpanded jets using parabolized Navier–Stokes equations and a variety of turbulence models

(Vatsa et al., 1981; Dash and Wolf, 1984a,b; Dash et al., 1985; Seiner et al., 1985; Cheuch et al., 1989). The compressibility-corrected version of the $k\varepsilon$ turbulence model predicts quite well the wavelength and amplitude of the pressure oscillations through the flow. However, predictions using the baseline turbulence model underestimate the wavelength of the pressure oscillation and overestimate their rate of decay in the streamwise direction at farther downstream. On the other hand, the solution of unsteady Euler equations to obtain the flowfield structures of underexpanded jets was also carried out by a number of researchers (Sinha et al., 1970; Prasad et al., 1994; Chen, 1998). The agreements between the predictions and experimental data were quite encouraging, especially at the near-field shock-containing region where the flow is largely inviscid. Nevertheless, the agreements were strongly dependent on the accuracy of the numerical schemes used. This fact suggests that high-order-accurate numerical schemes, both in space and in time, may help to gain a better understanding of the complex shock-wave interaction and the structure of the flowfield, and to furnish the lack of experimental measurements of turbulent properties in the near-field shock-containing region of imperfectly expanded supersonic jets.

In addition to the underexpanded supersonic jet, the spatially developing free shear layer generated by turbulent mixing of two fluid streams has been one of the most active researches in fluid mechanics and is encountered in many engineering applications. Incompressible planar free shear layers have been intensively investigated in the past with a substantial amount of material published on the mean flow quantities, turbulence properties, flow visualization, and development to self-similarity of the flow field (Winant and Browand, 1974; Brown and Roshko, 1974; Oster and Wygnanski, 1982). There has also been a great deal of experimental work in the area of compressible free shear layers. However, most experiments on compressible shear layers were limited to the mean flow measurements and the compressibility effects on the shear layer growth rate (Bogdanoff, 1983; Chinzei et al., 1986; Papamoschou and Roshko, 1988). Experiments demonstrated that the growth rate of mixing layer decreases with increasing convective Mach number (M_c). The convective Mach number is defined $M_c = (U_1 - U_c)/a_1$, where $U_c = (a_1U_2 + a_2U_1)/(a_1 + a_2)$. In addition to the mean flow and growth rate measurements, the turbulence properties for three convective Mach numbers ($M_c = 0.51$, 0.64, and 0.86) were added to provide rich experimental data for numerical schemes validations (Samimy and Elliott, 1990; Elliott and Samimy, 1990).

Numerical simulations on the spatially developing mixing layers have been reported using two subsonic (Grinstein et al., 1986; Sandham and Reynolds, 1989; Tsai and Christiansen, 1990) or two supersonic (Farouk et al., 1991; Lu and Wu, 1991) fluid streams. In contrast, the computation of mixing layers generated by an underexpanded supersonic and a subsonic stream has received less attention to date. This type of shear layer is often encountered in the practical ramjet combustor and is a subject of noise problem caused by discharging a supersonic jet into a subsonic stream. Although the computation of supersonic–subsonic mixing layer using high-order flux-corrected transport algorithm has been reported (Farouk et al., 1991), no quantitative comparison of the numerical results with available experimental data was made. This fact provides one of the motivations for the present study.

In the present study, the high-order weighted essentially non-oscillatory (WENO) finite-difference schemes (Jiang and Shu, 1996) are adapted to analyze an underexpanded supersonic air jet into still air and a supersonic–subsonic free shear layer. The present numerical model directly solves the governing equations without using subgrid-scale (SGS) turbulence models; consequently, the complexity of empirical turbulence models, especially those with compressibility-corrected terms, can be avoided. Although the present study solves the Euler equations without SGS turbulence models, numerical turbulence model inherent with numerical algorithm has been considered as a SGS model in many other investigations (Kailasanath et al., 1987, 1989; Jou and Riley, 1989; Oran and Boris, 1993). It has been demonstrated that the local, time-dependent numerical dissipation in the Euler equations behaves as a SGS turbulence model for scales smaller than grid sizes and this SGS model properly connects the large, energy-containing scales with the unresolved SGS of motion (Oran and Boris, 1993). In fact, the numerical dissipation is much more effective in the present study due to inherent high-dissipative nature of the WENO schemes. Numerical results are compared with existing experimental data for code validations. In addition, the physical mechanism responsible for the noise production in the underexpanded supersonic jet is discussed. The other objective of this study is to devise techniques for enhancing mixing and shock cells destruction in an underexpanded supersonic jet and to verify whether the jet noise suppression can be achieved.

2. Governing equations and numerical algorithm

Experimental (Seiner and Norum, 1979, 1980; Prasad et al., 1994) and numerical (Dash et al., 1985; Cheuch et al., 1989) results have confirmed that the flow is inviscid in the near-field shock-containing region of supersonic jets. In addition, the basic vortex dynamics in a shear layer is essentially inviscid (Ho and Huang, 1982; Grinstein et al., 1986). These findings suggest that the present simulations can be formulated using Euler equations.

2.1. Governing equations

The time-dependent, inviscid, compressible two-dimensional (2D) planar or axisymmetric Euler equations without body forces and external heat addition are written in conservation vector form as

$$\frac{\partial \boldsymbol{W}}{\partial t}+\frac{\partial \boldsymbol{F}}{\partial x}+\frac{\partial \boldsymbol{G}}{\partial y}+\alpha \boldsymbol{S}=0 \tag{1}$$

where $\alpha = 0$ represents 2D planar flow and $\alpha = 1$ represents 2D axisymmetric flow. The flux vectors in Eq. (1) are

$$\boldsymbol{W}=\begin{bmatrix}\rho\\ \rho u\\ \rho v\\ e\end{bmatrix},\quad \boldsymbol{F}=\begin{bmatrix}\rho u\\ \rho u^2+p\\ \rho uv\\ (e+p)u\end{bmatrix},\quad \boldsymbol{G}=\begin{bmatrix}\rho v\\ \rho uv\\ \rho v^2+p\\ (e+p)v\end{bmatrix},$$

$$\boldsymbol{S}=\frac{1}{y}\begin{bmatrix}\rho v\\ \rho uv\\ \rho v^2\\ (e+p)v\end{bmatrix} \tag{2}$$

The above governing equations represent the conservation of mass, momentum, and total energy of inviscid fluid motion. It is noted that the dimensional variables are used for free shear layer calculation, while the supersonic jet simulation uses dimensionless variables. Where t, p, ρ, u, v, and e are the time, pressure, density, x- and y-directional velocity components, and the total energy per unit mass, respectively. In terms of dimensionless variables, D (nozzle exit diameter) is the length scale, U_e (nozzle exit velocity) is the velocity scale, ρ_e (jet exit density) is the density scale, D/U_e is the time scale, and $\rho_e U_e^2$ is the pressure and total energy scales. For an ideal gas, the pressure is related to the equation of state

$$p=(\gamma-1)[e-0.5\rho(u^2+v^2)] \tag{3}$$

where γ (=1.4 for air) is the ratio of specific heats.

2.2. Numerical algorithm

In the computation of inviscid, compressible, under-expanded supersonic flow, the presence of infinitesimally thin shocks may lead to non-linear instability. Moreover, regions of strong gradients, which have finite thickness but are too thin for the grid to resolve, may also produce non-linear instability (Shu et al., 1992). Thus, the high-order, computationally stable across discontinuities numerical schemes are required. In this paper, the high-order weighted essentially non-oscillatory (WENO) schemes proposed by Jiang and Shu (1996) are applied to solve the time-dependent Euler equations. WENO schemes are based on ENO (essentially non-oscillatory) schemes, which were first introduced by Harten and Osher (1987) and Harten et al. (1987) in the form of cell averages. The key idea of ENO schemes is to use the smallest stencil among several candidates to approximate the fluxes at cell boundaries to a high-order accuracy and at the same time to avoid spurious oscillations near shocks. The cell-averaged version of ENO schemes involved a procedure of reconstructing point values from cell averages and could become complicated and costly for multi-dimensional problems. Later, Shu and Osher (1988, 1989) developed the flux version of ENO schemes, which does not require such a reconstruction procedure. ENO schemes are uniformly high order accurate right up to the shock and are very robust to use. However, they have certain drawbacks such as the freely adaptive stencil could change even by a round-off error perturbation near zeroes of the solution and its derivatives. To overcome these drawbacks, Liu et al. (1994) modified the cell averaged version of ENO schemes by using a convex combination of all the candidate stencils to approximate the numerical flux instead of using only one of the candidate stencils. Each of the candidate stencils is assigned a weight, which determines the contribution of this stencil to the final approximation of the numerical flux. Jiang and Shu (1996) modified and improved the WENO finite difference schemes of Liu et al. (1994) based on the flux version of ENO schemes. For more background on ENO and WENO schemes as well as their applications the reader is referred to the excellent works of Harten and Osher (1987), Harten et al. (1987), Shu and Osher (1988, 1989), Harten (1989), Rogerson and Meiberg (1990), Shu (1990), Shu et al. (1992), Liu et al. (1994), Jiang and Shu (1996), Xu et al. (1997), Pirozzoli (2004) and others.

2.3. Temporal integration and spatial discretization

To integrate the governing Euler equations, Eq. (1) can be rewritten as

$$\frac{\mathrm{d}\boldsymbol{W}}{\mathrm{d}t}=L(\boldsymbol{W})=-\boldsymbol{F}(\boldsymbol{W})_x-\boldsymbol{G}(\boldsymbol{W})_y-\alpha \boldsymbol{S}(\boldsymbol{W}) \tag{4}$$

where $L(\boldsymbol{W})$ is a discretization of the spatial operator. If the spatial dependence of $\boldsymbol{W}$ on x and r is known, then Eq. (4) can be regarded as an ordinary differential equation in time and can be solved by a Runge–Kutta scheme. The fourth-order time integration Runge–Kutta scheme is written as

$$\left.\begin{aligned}\boldsymbol{W}^{(1)}&=\boldsymbol{W}^n+\tfrac{1}{2}\Delta t L(\boldsymbol{W}^n)\\ \boldsymbol{W}^{(2)}&=\boldsymbol{W}^n+\tfrac{1}{2}\Delta t L(\boldsymbol{W}^{(1)})\\ \boldsymbol{W}^{(3)}&=\boldsymbol{W}^n+\Delta t L(\boldsymbol{W}^{(2)})\\ \boldsymbol{W}^{n+1}&=\tfrac{1}{3}[-\boldsymbol{W}^n+\boldsymbol{W}^{(1)}+2\boldsymbol{W}^{(2)}+\boldsymbol{W}^{(3)}]+\tfrac{1}{6}\Delta t L(\boldsymbol{W}^{(3)})\end{aligned}\right\} \tag{5}$$

where the superscript n denotes time step, $\boldsymbol{W}^{(i)}$ is the intermediate vectors with $i = 1$, 2, and 3, and Δt is the time increment.

For the discretization of a computational domain, the space is divided into uniform interval of size Δx and Δy with $x_i = i\Delta x$ and $y_j = j\Delta y$. The spatial operator, Eq. (4), can be numerically approximated as

$$L(\boldsymbol{W}) = -\alpha \boldsymbol{S}_{i,j} - \left[\frac{1}{\Delta x}(\tilde{\boldsymbol{F}}_{i+1/2,j} - \tilde{\boldsymbol{F}}_{i-1/2,j}) + \frac{1}{\Delta y}(\tilde{\boldsymbol{G}}_{i,j+1/2} - \tilde{\boldsymbol{G}}_{i,j-1/2})\right] \tag{6}$$

where $\boldsymbol{S}_{i,j}$ is the source term at the grid points and $\tilde{\boldsymbol{F}}_{i+1/2,j}$ and $\tilde{\boldsymbol{G}}_{i,j+1/2}$ denote interface fluxes in the x and y direction, respectively. High-order spatial discretization accuracy is achieved with high-order approximation of the flux function at cell interfaces. The distribution of interpolation points (stencil) is chosen according to the upwinding strategy of Lax–Friedrichs scheme. The numerical flux in the x direction is approximated using Lax–Friedrichs scheme that has the form

$$\tilde{\boldsymbol{F}}(\boldsymbol{W}) = \boldsymbol{F}^{+}(\boldsymbol{W}) + \boldsymbol{F}^{-}(\boldsymbol{W}) \tag{7}$$

where $\boldsymbol{F}^{+}$ and $\boldsymbol{F}^{-}$ satisfy $\frac{d\boldsymbol{F}^{+}}{d\boldsymbol{W}} \geqslant 0$ and $\frac{d\boldsymbol{F}^{-}}{d\boldsymbol{W}} \leqslant 0$. One choice for the positive and negative fluxes is

$$F^{\pm}(\boldsymbol{W}) = \frac{1}{2}(\boldsymbol{F}(\boldsymbol{W}) \pm \alpha \boldsymbol{W}), \quad \text{where } \alpha = \max|\boldsymbol{F}'(\boldsymbol{W})| \tag{8}$$

The flux at the interface is then defined by

$$\tilde{F}_{i+1/2,j} = \tilde{F}^{+}_{i+1/2,j} + \tilde{F}^{-}_{i+1/2,j} \tag{9}$$

To approximate $\tilde{F}^{+}_{i+1/2,j}$ and $\tilde{F}^{-}_{i+1/2,j}$ the fifth-order WENO scheme of Jiang and Shu (1996) is used in the present study. The approximation of $\tilde{\boldsymbol{F}}_{i-1/2,j}$, $\tilde{\boldsymbol{G}}_{i,j+1/2}$, and $\tilde{\boldsymbol{G}}_{i,j-1/2}$ is in a similar way.

2.4. Boundary and initial conditions for supersonic jet

The computational domain for an underexpanded supersonic jet is schematically shown in Fig. 1a. The non-dimensional nozzle length and nozzle diameter is $1D$. The flowfield is assumed to be axisymmetric. Hence, the computational domain covers $31D \times 5D$, which is extended from the nozzle exit and jet centerline by $30D$ and $5D$ in the axial and radial direction, respectively. The primitive variables (ρ, u, v, p) need to be specified at boundaries of the finite computational domain because they are involved in the flux vectors. For the case of supersonic inflow, the primitive variables are specified at the entrance (B1) due to four incoming characteristics. At the wall of nozzle (B2), the non-reflecting boundary conditions are imposed. In order to avoid shock waves reflecting from the ambient boundaries (B3 and B4), the Riemann invariants and entropy equation are enforced. At the jet centerline (B5), the primitive variables are assumed to be symmetry with $v = 0$ specified. At the exit plane (B6), there are four outgoing characteristics as the exit flow is supersonic and the outflow boundary conditions need not be specified. For the region of subsonic exit flow, the pressure is specified and the characteristic boundary conditions are imposed at the outflow plane since there are three outgoing characteristics and one incoming characteristic.

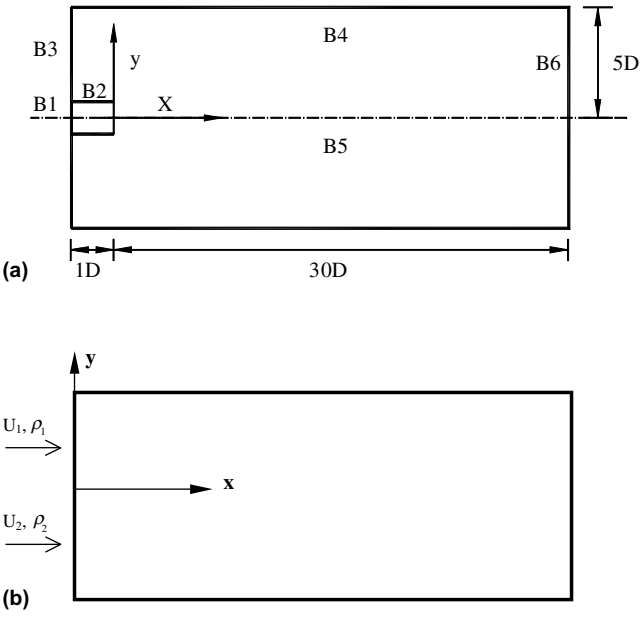

Fig. 1. Schematic diagram of the computational domain: (a) supersonic jet; (b) free shear layer.

The initial inlet conditions are specified based on the available experimental data of Seiner and Norum (1979, 1980) for a Mach 2 cold jet into atmospheric still air. The rest of computational domain is initially assumed to be in a still ambient environment. In order to induce the roll-up and pairing of vortex rings, the flow is imposed with a time-periodic, low-level amplitude inflow forcing. Because of the periodic inflow forcing, the evolution of jet flow proceeds with increasing time step and finally the jet approaches a periodic state. The jet was issued from a 50 mm exit diameter (D) of axisymmetric, convergent-divergent nozzle with design Mach number of 2 and the underexpanded static pressure ratio (p_e/p_a) was 1.45. The stagnation and the still air temperatures were assumed to be 288 K. The calculated nozzle exit velocity was 507 m/s. Four sets of uniform grid—310×70, 500×110, 625×140, and 730×160 $(x \times y)$ are used for the grid-independence study and the grid independence is attained for grid sizes of 625×140 and 730×160. The deviations in streamwise static pressure variation calculated from these two grid systems are less than 3%. Thus the grid size of 625×140 is then used for the rest of supersonic jet studies. In addition, a computational domain of $41D \times 10D$ with the grid size of

827×280 is also used for a test run. The deviations in streamwise static pressure variation calculated from $41D \times 10D$ and $31D \times 5D$ are less than 5%. Therefore, far-field assumptions for the computational domain of $31D \times 5D$ were reasonable. All the statistical data presented for supersonic jet are obtained by averaging over an appropriate period of time ($100 \leqslant t^* \leqslant 125$).

2.5. Boundary and initial conditions for free shear layer

The computational domain of the mixing layer is schematically shown in Fig. 1b. The splitter plate is not included in the computational domain and its trailing edge forms the left boundary of the computational domain. In order to avoid the expansion or compression waves generated at the trailing edge of the splitter plate reflecting from the upper boundary, the Riemann invariants and entropy equation are imposed at the upper boundary. The lower boundary is assumed to be streamline and the numerical boundary conditions are specified as $v = 0$ and $\partial w/\partial y = 0$, where w is ρ, u, or e. At the exit plane, the boundary conditions are specified as those of supersonic jet. At the inlet plane, both mass and energy flux are kept constant. A hyperbolic-tangent velocity profile is adopted for the initial streamwise velocity distribution at the splitter plate as

$$u(y) = \overline{U}\left[1 + \frac{1-\lambda_u}{1+\lambda_u}\tanh\left(\frac{y}{2\theta_0}\right)\right] \tag{10}$$

where $\overline{U} = (U_1 + U_2)/2$ is the average of two stream velocities, $\lambda_u = U_2/U_1$ is the velocity ratio, and θ_0 is the initial momentum thickness. In order to produce the roll-up and pairing of vortex rings, an unsteady boundary condition is also applied at the inlet plane, i.e.,

$$v(y,t) = \Delta U G(y) \sum_{m=0}^{3} A \sin(2\pi f_m t + \phi_m) \tag{11}$$

where $\Delta U = (U_1 - U_2)$ is the difference of two stream velocities which measures the strength of shearing, $G(y)$ is a Gaussian function which has a peak value of unity at $y = 0$ and half width over eight cells, $A = 0.001$ is the forcing amplitude, f_m is the fundamental frequency and its first three subharmonics, and ϕ_m is the random phases added (Sandham and Reynolds, 1989). The forcing is modified by introducing these random phases to the Rayleigh modes so that the pairing of two vortices will occur randomly in space and in time during the course of simulation.

The initial inlet conditions are specified based on the available experimental data of Samimy and Elliott (1990) for the underexpanded case. The inflowing upper and lower stream Mach number is 1.96 and 0.37, respectively. The mixing layer is formed at the velocity ratio $U_2/U_1 = 0.25$ and density ratio $\rho_2/\rho_1 = 9.58$. The convective Mach number of the mixing layer for this case is 0.64. By analogy to supersonic jet, an underexpanded shear layer is simulated as the one in which the pressure of the faster stream is higher at the entrance than that of the slower stream. The computation domain is set to be 60 cm long and 30 cm high to meet the far-field assumptions. Three sets of uniform grid—425×200, 525×240, and 625×140 ($x \times y$) are used for the grid-independence study and the grid independence is attained for grid sizes of 525×240 and 625×140. The deviations in the axial mean velocity and turbulence quantities calculated from these two grid systems are less than 4%. Thus the grid size of 525×240 is then used for the rest of shear layer studies. All the statistical data presented for shear layer are obtained by averaging over an appropriate period of time.

3. Results and discussion

3.1. Characteristics of underexpanded jet

Comparisons of the calculated streamwise mean static pressure variations along the jet centerline with the measurements of Seiner and Norum (1979, 1980) are illustrated in Fig. 2. The calculated results of Dash

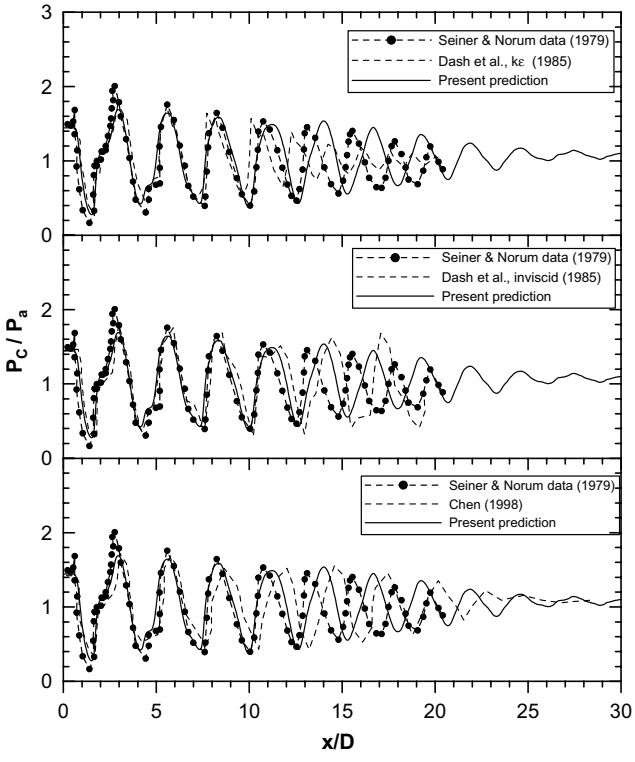

Fig. 2. Comparison of predicted and measured mean streamwise pressure variations along axis in the underexpanded jet. The predictions of Dash et al. (1985) using various types of turbulence models and Chen (1998) using different numerical schemes are also shown in the figure for comparison.

et al. (1985) using $k\varepsilon$ model and the inviscid solution are also shown in the figure for comparison. Both prediction and measurement exhibit the decaying oscillatory static pressure variations caused by the interaction between the shock cells and the mixing layers near the edge of the flow. The present simulation agrees quite well with the experiment for the first five shock cells, where the flow is largely inviscid. The slight difference between the measured and calculated data beginning with the sixth shock cell is mainly due to the fact that present calculation underestimates a rate of mixing between the jet and ambient fluid at farther downstream. The predicted results of Dash et al. (1985) indicate that the $k\varepsilon$ model predicts too fast a rate of mixing and, hence, foreshortens the cell lengths and dampens the wave strengths prematurely. However, the inviscid solution predicts no wave damping or cell foreshortening. Comparisons of present calculation with the predicted result of Chen (1998) as well as the experiment of Seiner and Norum (1979, 1980) are also shown in Fig. 2. Chen (1998) used the modified Osher and Chakravarthy (MOC) finite volume scheme to solve the time-dependent Euler equation for the same problem. The MOC scheme predicted the decaying oscillatory static pressure variation but with too slow a rate of mixing. Comparisons of the present simulation using the WENO scheme with that of Dash et al. (1985) and Chen (1998) using different algorithms demonstrate that the WENO scheme can properly

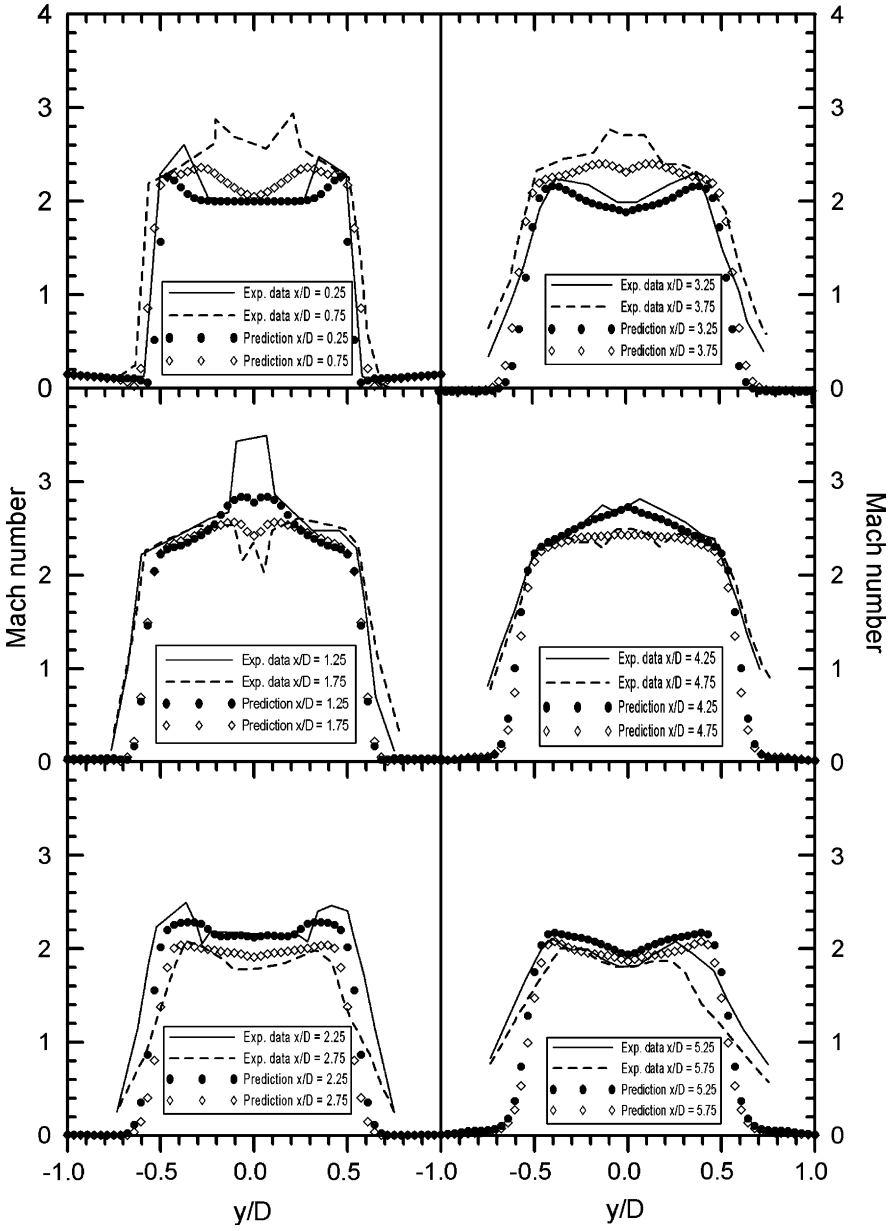

Fig. 3. Comparison of predicted and measured radial distribution of Mach number at various axial positions in the underexpanded jet.

model the strong shock-containing region of an underexpanded supersonic jet even without including turbulence models. Also, the WENO scheme predicts the static pressure variation more properly than the MOC scheme dose, because higher order integration methods, both in time and in space, are used in the WENO scheme. These facts indicate that the code is valid for analyzing the inviscid imperfectly expanded supersonic jets.

Comparisons of the predicted and measured radial distributions of Mach number are shown in Fig. 3. In general, the calculations are in good agreement with the experimental data of Seiner and Norum (1979). The locations of the discontinuities in the flow are properly captured, and they are evident in the figure. The underprediction of the Mach number around the jet center and near the outer radial region is because that a parallel nozzle flow is assumed in the simulation while a converging–diverging nozzle was used in the experiment. Since the converging–diverging nozzle expands jet plume to an outer radial region than does a tube nozzle, thus it causes a slower decaying rate of the Mach number in the jet boundary. Both measured and calculated data indicate that normal shocks are not present in near field of this underexpanded flow because the Mach numbers are higher than unity.

To better understand the flowfield of an underexpanded jet, the instantaneous flow pictures of density,

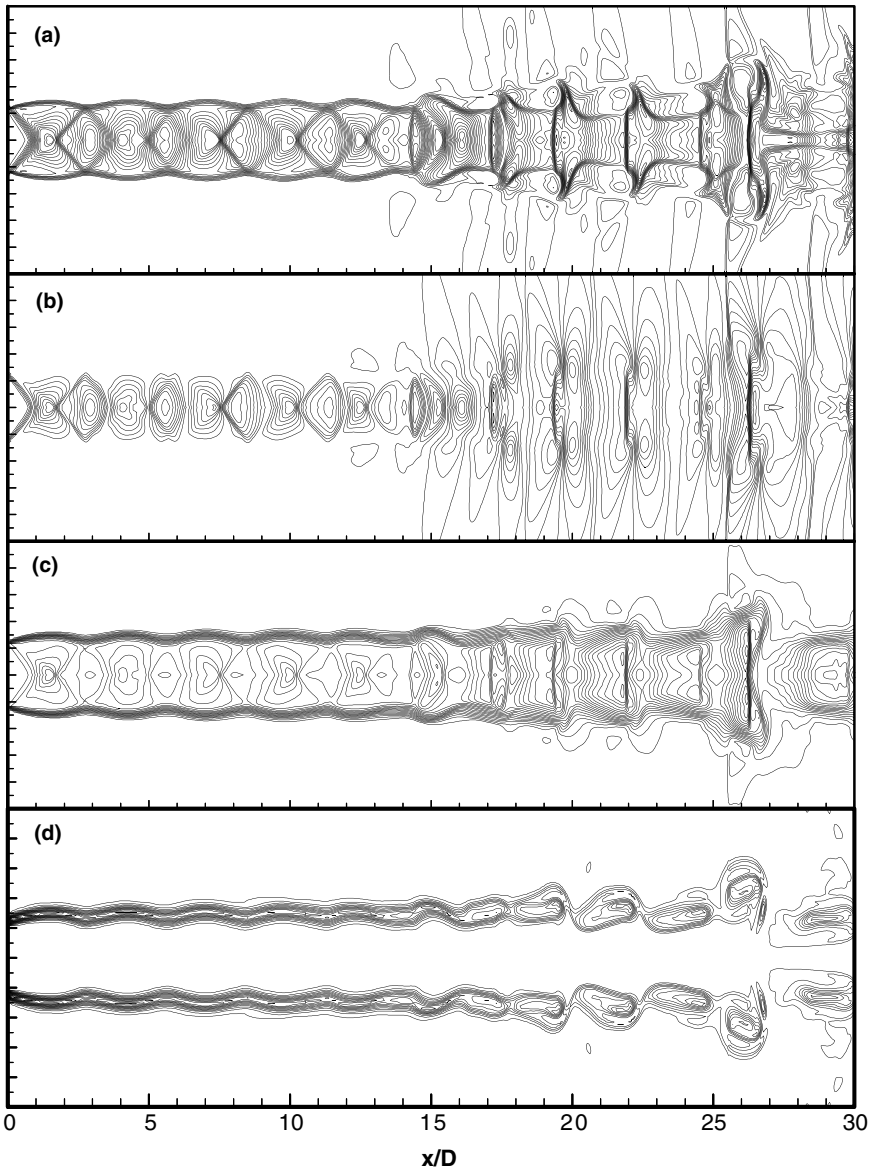

Fig. 4. Instantaneous flow pictures for the underexpanded jet at $t = 125$: (a) density (contour lines from 0.26 to 1.11, increment 0.04); (b) pressure (contour lines from 0.04 to 0.24, increment 0.01); (c) Mach number (contour lines from 0.24 to 2.94, increment 0.15); (d) vorticity (contour lines from –3.48 to 14.78, increment 0.68). The radial coordinate has been magnified by a factor of 2.5.

pressure, Mach number, and vorticity at a representative instant $t = 125$ are shown in Fig. 4. Fig. 4a and b illustrate the density and pressure contour lines, in which Prandtl–Meyer expansion fans originally formed at the nozzle lip reflect back and forth between the jet centerline and the free shear layer to form oblique shock and expansion wave systems (diamond-shape shock cells). The repeated shock cells extend to further downstream and die out at $x/D = 25$ due to entrainment of the ambient air into the jet. The Mach number contour lines indicate that no normal shocks exist in the near field of shock containing region (Fig. 4c). Fig. 4d shows that there is essentially no mixing occurred between the jet boundary and ambient air at $x/D < 17$, due to compressibility effects in this high-convective Mach number (0.94) flow. As the vortices are convected downstream, they draw energy from the jet and grow in strength. The vortex roll-up starts at $x/D > 17$ and finally becomes large-scale structures in the far downstream. It is noted that the growth of the shear-layer vortices is relatively weak compared to subsonic jets (Chao and Chou, 1998). As a result, this would impede its applications to supersonic combustion in which mixing of fuel and oxidizer is extremely important.

In addition to lower mixing rate, another important feature of supersonic jet is the shock-associated noise. Shock noise from supersonic jets can contain two components: one is the high-amplitude discrete tone, called screech, and the other is broadband in nature. Powell (1953) inferred the mechanism of screech generation to be the acoustic feedback of noise generated by the passage of disturbances through a shock that resulted in additional disturbances being created at the nozzle exit. The broadband shock noise is related to the interaction of the turbulent mixing layer with a stationary set of shock cells (Seiner and Norum, 1980). In the present study, the time averaged sound pressure level (SPL) generated from the underexpanded supersonic jet is shown in Fig. 5. The SPL is defined as

$$\mathrm{SPL(dB)} = 20\log_{10}(p'_{\mathrm{rms}}/p_{\mathrm{ref}}) \tag{12}$$

where p'_{rms} is the root mean square pressure fluctuation and $p_{\mathrm{ref}} = 20$ μPa is the commonly used reference pressure. Fig. 5 indicates that the noise is originally generated from the shock cell and radiates in the direction of 40°–50° to the jet axis. The SPL increases with increasing downstream locations. In order to identify the source of shock noise, the pressure variations at seven downstream locations are monitored for a time interval of $t = 100$–125 and analyzed using Fast Fourier Transforms. The power spectral densities for seven locations $(x, y$: $3D, 0D$; $10D, 0D$; $15D, 0.5D$; $20D, 0.5D$; $25D, 0D$; $2D, 3.5D$; $0D, 4D)$ are shown in Fig. 6. For

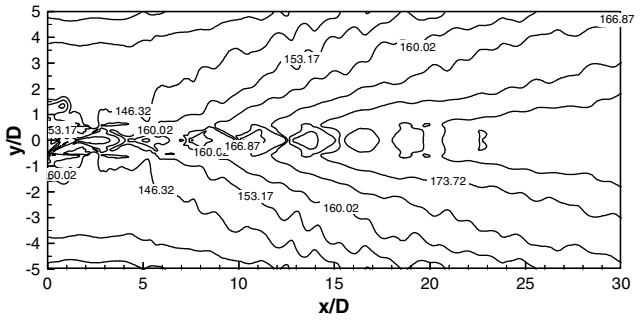

Fig. 5. The SPL (dB) contour of the underexpanded jet.

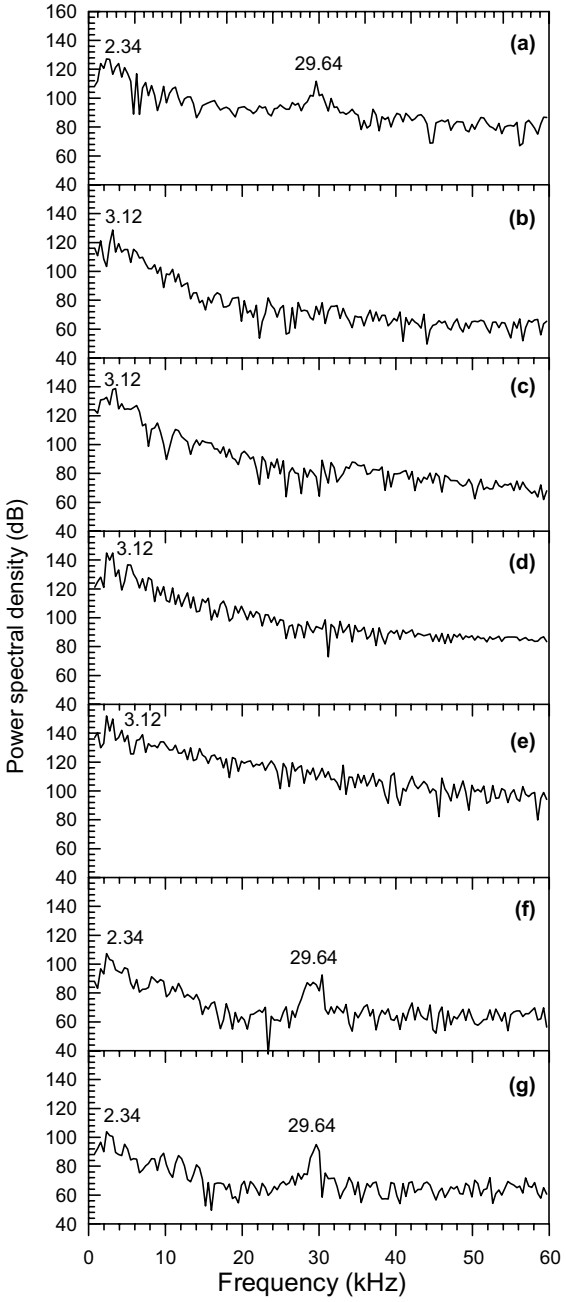

Fig. 6. Power spectral density of the underexpanded jet at several downstream locations (x, y). (a) $(3D, 0D)$, (b) $(10D, 0D)$, (c): $(15D, 0.5D)$, (d) $(20D, 0.5D)$, (e) $(25D, 0D)$, (f) $(2D, 3.5D)$, (g) $(0D, 4D)$.

the locations away from the jet exit (Fig. 6b–e), either at the jet center or at the mixing layer, there is only one peak frequency occurred at 3.12 kHz. The spectrum indicates that its amplitude rises rapidly with frequency to a well-defined peak, and then decreases at higher frequency. This low frequency peak is believed to be due to the interaction of mixing layer with a stationary set of shock cells, and hence classified as the broadband shock noise. For the locations near the jet exit (Fig. 6a, f, and g), in addition to a low frequency peak occurred at 2.34 kHz, there is an unusual second peak appeared at a frequency of 29.64 kHz. The cause of this high-frequency peak is unknown. However, it only appears at locations near the nozzle exit and could be due to resonant oscillation of the shock cell structure that produces the screech tones.

3.2. Forcing of the underexpanded jet

The calculations of underexpanded jet demonstrate that there is essentially no mixing between the jet and ambient air in the near-field shock-containing regions. This would impede its future applications to supersonic combustion engines and also generate very high level of noise. Previous experimental studies in subsonic shear layer growth rate have demonstrated that the shear layer growth rate can be altered markedly by introducing external perturbations near the point of initial mixing (Ho and Huang, 1982; Oster and Wygnanski, 1982). It is interesting to examine whether the same concepts are still effective for achieving the mixing enhancement and noise reduction in supersonic jet. Fig. 7 shows the effect of various types of forcing on the streamwise development of momentum thickness for the underexpanded jet under a sinusoidal normal velocity disturbance at the nozzle tip, which includes various forms of forcings excited at the fundamental frequency (f_0) and its first subharmonics (f_1), each with an amplitude of 5% nozzle exit velocity. The type of forcing is similar to that described in Eq. (11). The momentum thickness is defined as

$$\theta = \int_0^\infty \frac{\rho(x,r)}{\rho(x,0)} \frac{u(x,r)}{u(x,0)} \left[1 - \frac{u(x,r)}{u(x,0)}\right] \mathrm{d}r \tag{13}$$

Fig. 7 shows that for two forcing cases, the inflow excitation increases the growth of the momentum thickness markedly as compared with the unforced case. A step-like increase of the momentum thickness is observed for all forcing cases at $x/D \approx 7$. The negative momentum thickness is due to integration of Eq. (13) over the regions where expansion waves accelerate the axial velocity to exceed the centerline velocity. Fig. 7 clearly demonstrates that the inflow excitation has pronounced effects on the supersonic jet; in turn, it can effectively manipulate the spreading rate of the mixing layer and hence achieves mixing enhancement.

In addition to mixing enhancement, the inflow excitation can also destruct the shock cells through enhanced entrainment and mixing. The destruction of the shock cells is represented by the decay of the centerline pressure variations as shown in Fig. 8. The forcings increase the centerline pressure at the nozzle exit but decrease the pressure variation very quickly after the second shock-cell. In order to examine whether the forcing can also effectively reduce the jet noise, the SPL contour at various forcing frequencies is shown in Fig. 9. For both forcing cases, the low level noise is generated from the shock cells near the nozzle exit, while the high-level noise is produced from the large vortices and breakup eddies and enveloped by the low level noise. The overall SPL for the forced cases is about 10–20 dB higher than

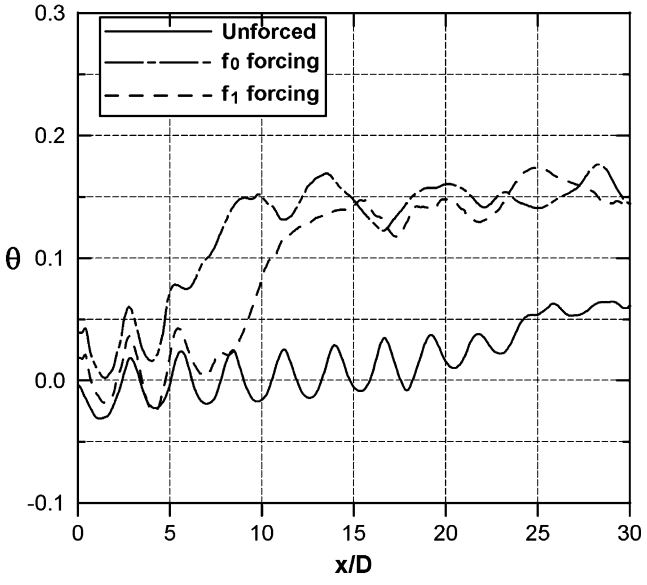

Fig. 7. Axial variations of momentum thickness for the underexpanded jet with various types of forcings.

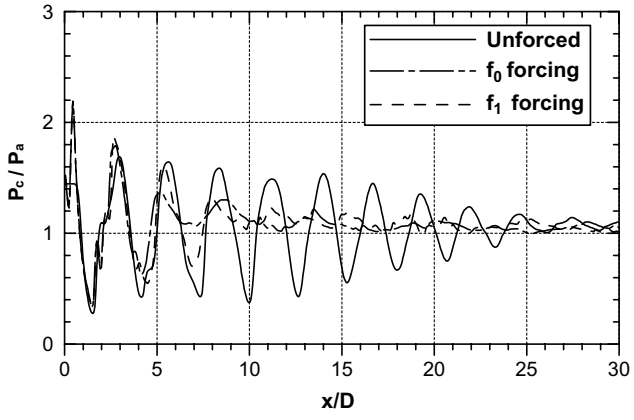

Fig. 8. Axial variations of mean static pressure for the underexpanded jet with various types of forcings.

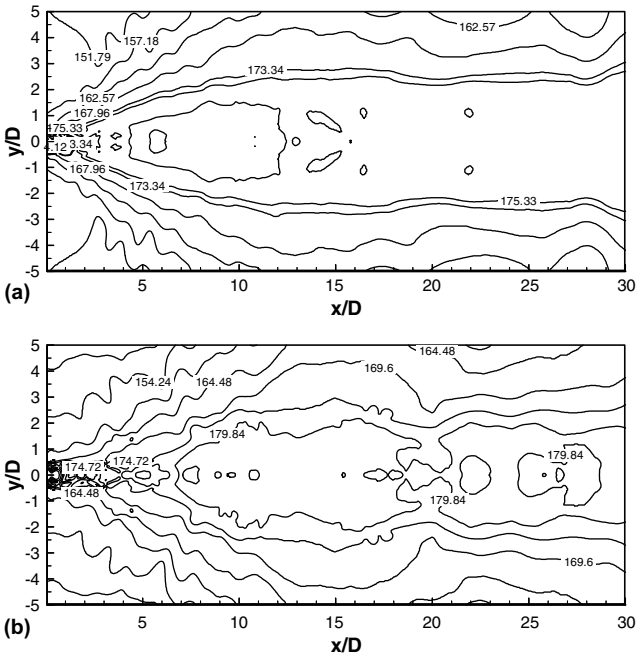

Fig. 9. The SPL (dB) contour of the underexpanded jet at various forcing frequencies: (a) forced with f_0, (b) forced with f_1.

the unforced case. The pressure variations at seven downstream locations (same as the unforced case) are also monitored for a time interval of $t = 100$–125 and analyzed using Fast Fourier Transforms. The power spectral densities for seven locations are shown in Fig. 10. Fig. 10 indicates that the forcing can modify or eliminate the high-frequency peak near the nozzle exit (Fig. 10a, f, and g). However, the overall noise level is also increased by about 10–20 dB. The method of enhancing mixing and shock-cell destruction in a supersonic jet may offer an opportunity of improving the performance of mixing in the related engineering applications but with a shortcoming of extra noise production.

3.3. Characteristics of free shear layer

The sequence of instantaneous flow visualization of the density and vorticity field for the underexpanded shear layer ($M_c = 0.64$) is shown in Figs. 11 and 12, respectively. Several features are found from these figures. The sheared fluid results in deeper incursions from the high-speed side into the low-speed side. These numerical snapshots clearly show the pairing phenomenon between two adjacent vortices. Calculations ratify that after the merging interactions among neighboring eddies, the newly formed large vortex convects downstream at nearly constant speed which is approximately the average of the two free stream velocities. This vortex amalgamation process occurs randomly in space and time which is responsible for the linear growth of the mixing layer. The spacing between two adjacent vortices

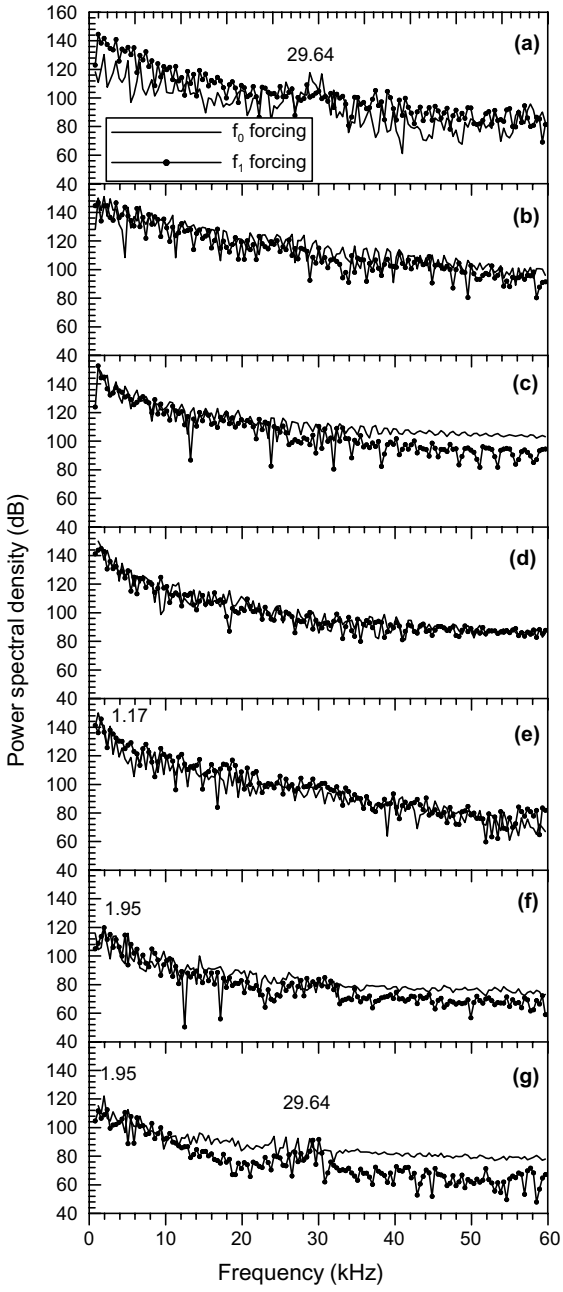

Fig. 10. Power spectral density of the forced underexpanded jet at several downstream locations (x, y). (a) $(3D, 0D)$, (b) $(10D, 0D)$, (c) $(15D, 0.5D)$, (d) $(20D, 0.5D)$, (e) $(25D, 0D)$, (f) $(2D, 3.5D)$, (g) $(0D, 4D)$.

and the size of vortex are increasing with the streamwise coordinate.

Comparisons of the calculated distributions of axial mean velocity, axial variation of the momentum and vorticity thicknesses, and turbulence quantities with the experimental data (Samimy and Elliott, 1990; Elliott and Samimy, 1990) are depicted in Figs. 13–15. The non-dimensional variables used in the figures, such as $U^* = (\bar{u} - U_2)/(U_1 - U_2)$, $y^* = (y - y_0)/\delta_w$,

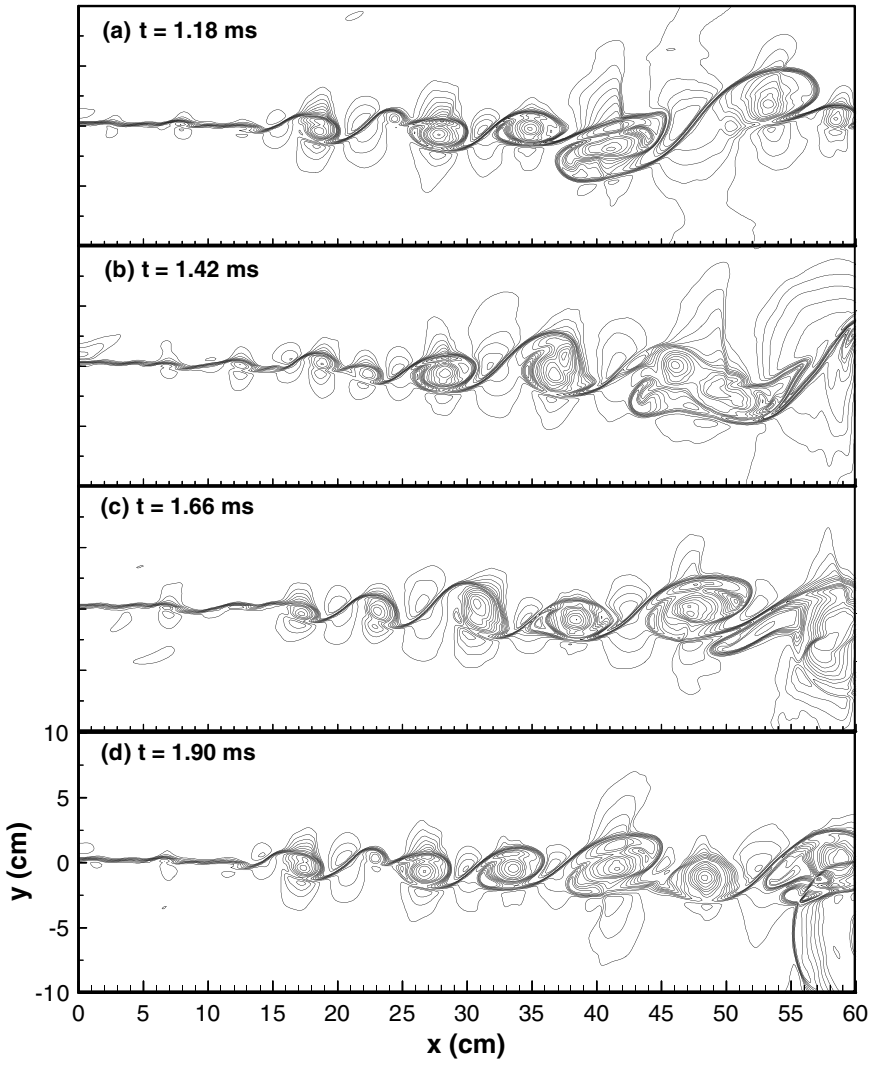

Fig. 11. Evolution of density at various instantaneous times for the $M_c = 0.64$ shear layer.

$\theta = \int_{-\infty}^{+\infty} (\bar{\rho}/\rho_1) U^*(1 - U^*)\,\mathrm{d}y$, and $\delta_w = (U_1 - U_2)/(\partial \bar{u}/\partial y)_{\max}$, are defined as in the experiments. The lateral distributions of the normalized streamwise mean velocity at four axial positions as shown in Fig. 13 suggest that the mean flow is self-similar in the fully developed region for $x \geqslant 12$ cm. The calculated results are in excellent agreement with the experimental data. Fig. 14 indicates that the shear layer growth in terms of momentum and vorticity thickness is predicted reasonably accurate by the present numerical method, as compared to experimental measurements. Further comparison of the calculated results with experimental data is shown in Fig. 15a–c for the development of the streamwise and lateral turbulence intensities, and Reynolds stress, respectively. Fig. 15 indicates that the computed turbulence quantities appear to collapse only for $x \geqslant 15$ cm, which shows that the turbulence similarity is achieved further downstream than the mean flow similarity. The calculated turbulence properties are also in good agreement with the experimental measurements except the lateral turbulence intensities. The maximum fluctuations of lateral turbulence intensities that are slightly off $y^* = 0$ position may be due to three-dimensional effects at high-convective Mach numbers (Sandham and Reynolds, 1991). The characteristic bell shape of the distribution of the turbulence quantities reveals that the self-similarity feature is still present in a supersonic–subsonic mixing layer.

4. Conclusions

The flowfield structures and properties of underexpanded cold jet and free shear layer have been computed by numerical solution of the compressible Euler equations. The high-order weighted essentially non-oscillatory (WENO) finite-difference schemes have shown their ability to overcome the numerical oscillations

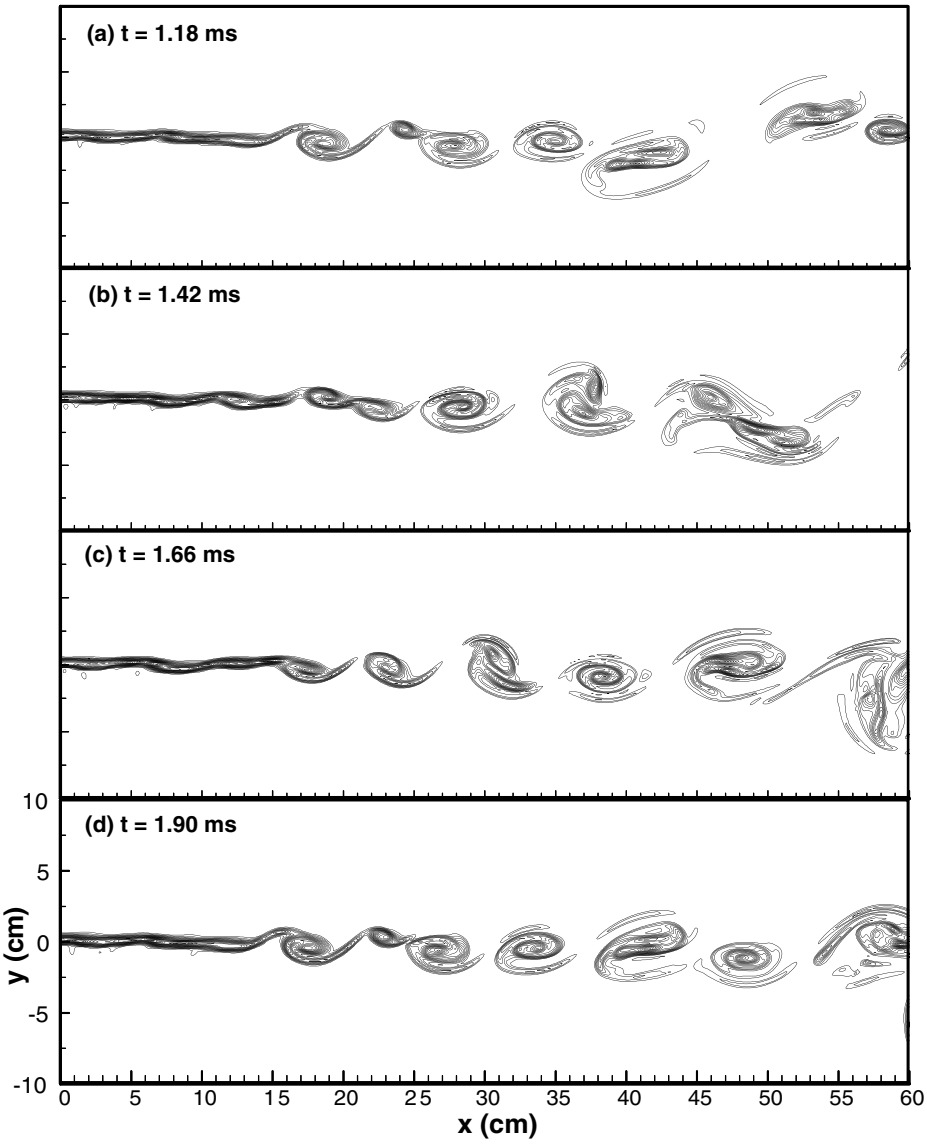

Fig. 12. Evolution of vorticity at various instantaneous times for the $M_c = 0.64$ shear layer.

across the shock cells in the flows. Good agreement between the predicted and available experimental data has been demonstrated in the near-field shock-containing region of underexpanded jet. The numerical flow visualization of the density, pressure, Mach number, and vorticity fields facilitates a systematic understanding of the streamwise evolution of flow structures under underexpanded condition. The calculated SPL contour indicates that the jet noise is generated from the shock cells and radiates in the direction of 40°–50° to the jet axis, which results in broadband shock noise. The computed results of an underexpanded jet indicate that the near-field region of the jet is influenced by compressibility, which reduces turbulent mixing rate and suppresses vortex roll-up and pairings. Improvement of the mixing can be achieved with an internal excitation by destruction the shock cells. This mechanism would offer an opportunity of improving the performance in the related engineering applications but with a drawback of extra noise production.

The numerical flow visualization of the density and vorticity fields and the associated turbulence quantities calculations are also demonstrated for an underexpanded mixing layer at high-convective Mach number. A detailed quantitative comparison between the present computation and reported experimental data indicates that the numerical turbulence model inherent with WENO algorithm can satisfactorily predict turbulence properties even without including SGS turbulence models. In the future, further implement of the viscous terms

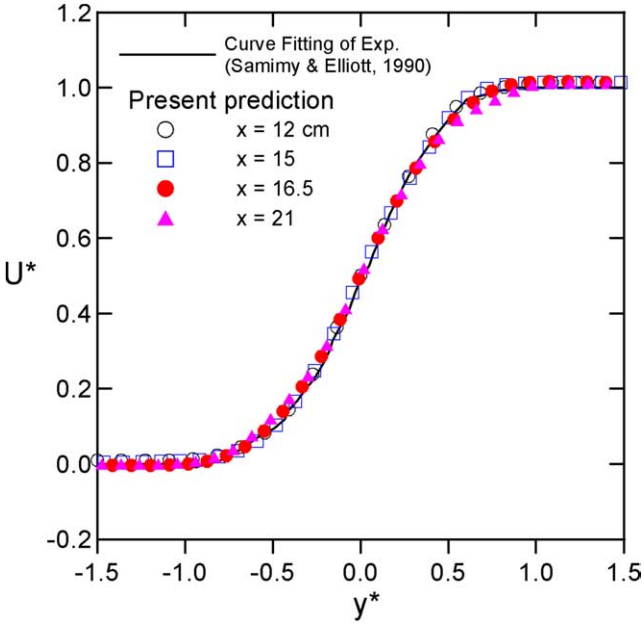

Fig. 13. Comparison of predicted and measured axial mean velocity profiles at four axial positions in the shear layer.

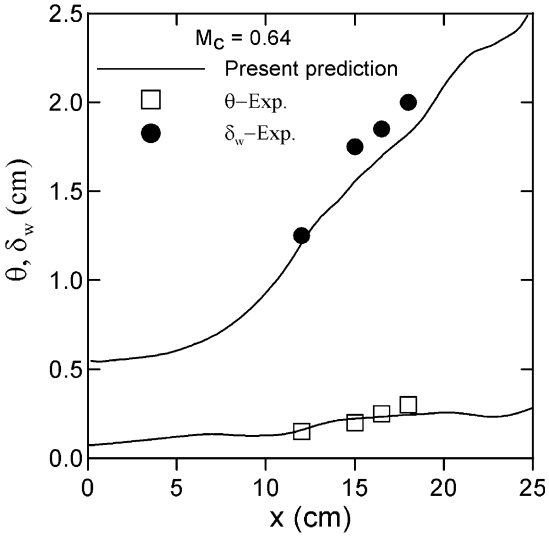

Fig. 14. Comparison of predicted and measured momentum and vorticity thickness along the axial direction in the shear layer.

into the code may improve the prediction of pressure variations in the far-field regions of the underexpanded jet. Also, a simple Smagorinsky subgrid model will be included to test the difference between SGS model and present numerical turbulence model.

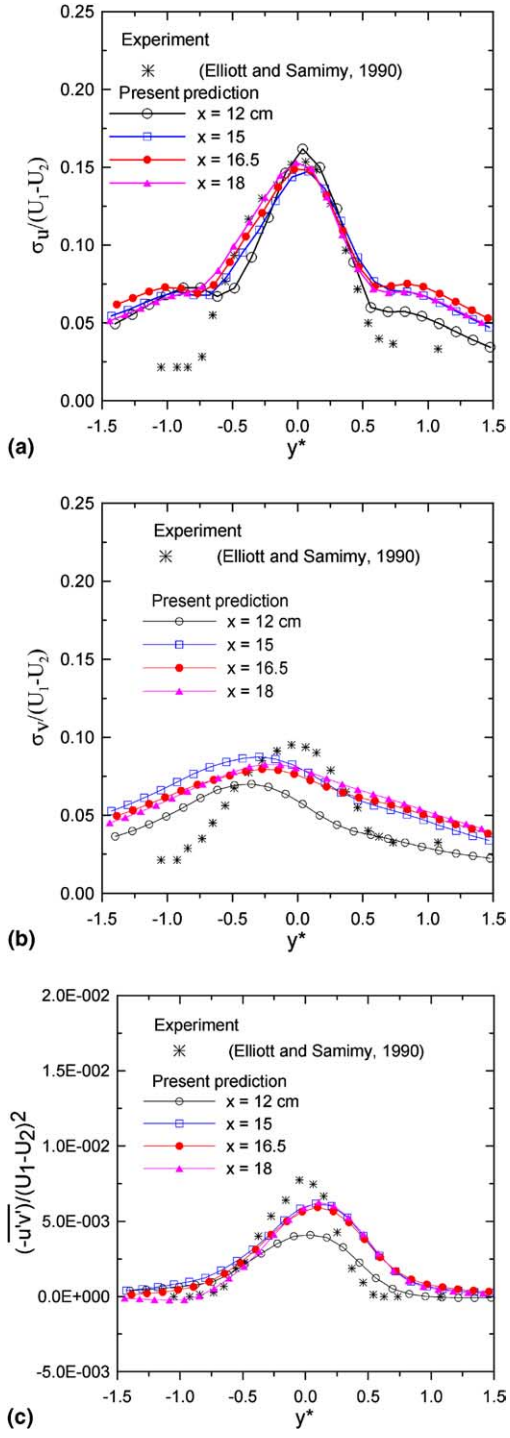

Fig. 15. Comparison of predicted and measured turbulence quantities at four axial positions in the shear layer. (a) Streamwise turbulent intenisty, (b) Lateral turbulent intensity and (c) Reynolds stress.

Acknowledgements

This work was partially supported by the National Science Council of the Republic of China, Grant No. NSC 88-2212-E-216-006, and computer time was provided by the National Center For High-Performance Computing. The authors gratefully acknowledge Professor S.-Y. Lin of National Cheng Kung University, Taiwan, ROC, for many fruitful discussions.

References

Adamson Jr., T.C., Nicholls, J.A., 1959. On the structure of jets from highly underexpanded nozzles into still air. J. Aeronaut. Sci. 26, 16–24.

Addy, A.L., 1981. Effects of axisymmetric sonic nozzle geometry on Mach disk characteristics. AIAA J. 19, 121–122.

Birch, A.D., Brown, D.R., Dodson, M.G., Swaffield, F., 1984. The structure and concentration decay of high pressure jets of natural gas. Combust. Sci. Technol. 36, 249–261.

Bogdanoff, D.W., 1983. Compressibility effects in turbulent shear layers. AIAA J. 21, 926–927.

Brown, G.L., Roshko, A., 1974. On the density effects and large structures in turbulent mixing layers. J. Fluid Mech. 64, 775–816.

Chao, Y.-C., Chou, W.-F., 1998. Simpler-based procedure for numerical simulation of dynamic vortical characteristics of some turbulent flows. Numer. Heat Transfer B 33, 37–64.

Chen, K.-C., 1998. Numerical simulation and noise suppression of high speed jets. Ph.D. Thesis. Institute of Aeronautics and Astronautics, National Cheng Kung University, Tainan, Taiwan, ROC.

Cheuch, S.G., Lai, M.-C., Faeth, G.M., 1989. Structure of turbulent sonic underexpanded free jets. AIAA J. 27, 549–559.

Chinzei, N., Masuya, G., Komuro, T., Murakami, A., Kudou, K., 1986. Spreading of two-stream supersonic turbulent mixing layers. Phys. Fluids 29, 1345–1347.

Crist, S., Sherman, P.M., Glass, D.R., 1966. Study of the highly underexpanded sonic jet. AIAA J. 4, 68–71.

Dash, S.M., Wolf, D.E., 1984a. Interactive phenomena in supersonic jet mixing problems, part I: phenomenology and numerical modeling techniques. AIAA J. 22, 905–913.

Dash, S.M., Wolf, D.E., 1984b. Interactive phenomena in supersonic jet mixing problems, part II: numerical studies. AIAA J. 22, 1395–1404.

Dash, S.M., Wolf, D.E., Seiner, J.M., 1985. Analysis of turbulent underexpanded jets, part I: parabolized Navier–Stokes model, SCIPVIS. AIAA J. 23, 505–514.

Davidor, W., Penner, S.S., 1971. Shock standoff distances and Mach-disk diameters in underexpanded sonic jets. AIAA J. 9, 1651–1653.

Dolling, D.S., Fournier, E., Shau, Y.R., 1990. Effects of vortex generators on the growth rate of a compressible turbulent shear layer. AIAA paper 90-1979.

Elliott, G.S., Samimy, M., 1990. Compressibility effects in free shear layers. Phys. Fluids A 2, 1231–1240.

Ewan, B.C.R., Moodie, K., 1986. Structure and velocity measurements in underexpanded jets. Combust. Sci. Technol. 45, 275–288.

Farouk, B., Oran, E.S., Kailasanath, K., 1991. Numerical simulations of the structure of supersonic shear layers. Phys. Fluids A 3, 2786–2798.

Gore, J.P., Faeth, G.M., Evans, D., Pfenning, D.B., 1986. Structure and radiation properties of large-scale natural gas/air diffusion flames. Fire Mater. 10, 161–169.

Grinstein, F.F., Oran, E.S., Boris, J.P., 1986. Numerical simulations of asymmetric mixing in planar shear flows. J. Fluid. Mech. 165, 201–220.

Harten, A., Osher, S., 1987. Uniformly high-order accurate nonoscillatory schemes I. SIAM J. Numer. Anal. 24, 279–309.

Harten, A., Engquist, B., Osher, S., Chakravarth, S., 1987. Uniformly high order accurate essentially non-oscillatory schemes III. J. Comput. Phys. 71, 231–303.

Harten, A., 1989. ENO scheme with subcell resolution. J. Comput. Phys. 83, 148–184.

Ho, C.-M., Huang, L.-S., 1982. Subharmonics and vortex merging in mixing layers. J. Fluid. Mech. 119, 443–473.

Hu, H., Saga, T., Kobayashi, T., Taniguchi, N., 2000. Passive control on jet mixing flows by using vortex generators. In: Proceedings of the 6th Triennial International Symposium on Fluid Control, Measurement and Visualization, Sherbrooke, Canada.

Jiang, G.-S., Shu, C.-W., 1996. Efficient implementation of weighted ENO schemes. J. Comput. Phys. 126, 202–228.

Jou, W.H., Riley, J.J., 1989. Progress in direct numerical simulations of turbulent reacting flows. AIAA J. 27, 1543–1556.

Kailasanath, K., Gardner, J.H., Boris, J.P., Oran, E.S., 1987. Numerical simulations of acoustic–vortex interactions in a central-dump ramjet combustor. J. Propul. Power 3, 525–533.

Kailasanath, K., Gardner, J.H., Boris, J.P., Oran, E.S., 1989. Acoustic–vortex interactions and low-frequency oscillations in axisymmetric combustor. J. Propul. Power 5, 165–171.

Liu, X.-D., Osher, S., Chan, T., 1994. Weighted essentially non-oscillatory schemes. J. Comput. Phys. 115, 200–212.

Lu, P.J., Wu, K.C., 1991. Numerical investigation on the structure of a confined supersonic mixing layer. Phys. Fluids A 3, 3063–3079.

Oran, E.S., Boris, J.P., 1993. Computing turbulent shear flows – a convenient conspiracy. Comput. Phys. 7, 523–533.

Oster, D., Wygnanski, I., 1982. The forced mixing layer between parallel streams. J. Fluid Mech. 123, 91–130.

Papamoschou, D., Roshko, A., 1988. The compressible turbulent shear layer: an experimental study. J. Fluid Mech. 197, 453–477.

Pirozzoli, S., 2004. Dynamics of ring vortices impinging on planar shock waves. Phys. Fluids 16, 1171–1185.

Powell, A., 1953. On the mechanism of choked jet noise. Proc. Phys. Soc. B. 66, 1039–1056.

Prasad, J.K., Mehta, R.C., Sreekanth, A.K., 1994. Impingement of supersonic jets on an axisymmetric deflector. AIAA J. 32, 1535–1538.

Rogerson, A., Meiberg, E., 1990. A numerical study of the convergence properties of ENO schemes. J. Sci. Comput. 5, 151–167.

Samimy, M., Elliott, G.S., 1990. Effects of compressibility on the characteristics of free shear layers. AIAA J. 28, 439–445.

Samimy, M., Zaman, K.B.M.Q., Reeder, M.F., 1993. Effect of tabs on the flow and noise field of an axisymmetric jet. AIAA J. 31, 609–619.

Sandham, N.D., Reynolds, W.C., 1989. Some inlet-plane effects on the numerically simulated spatially developing plane mixing layer. In: Turbulent Shear Flow, 6. Springer-Verlag, Berlin, pp. 441–453.

Sandham, N.D., Reynolds, W.C., 1991. Three-dimensional simulations of large eddies in the compressible mixing layer. J. Fluid Mech. 224, 133–158.

Seiner, J.M., Norum, T.D., 1979. Experiments of shock associated noise on supersonic jets. AIAA paper 79-1526.

Seiner, J.M., Norum, T.D., 1980. Aerodynamic aspects of shock containing jet plumes. AIAA paper 80-0965.

Seiner, J.M., Dash, S.M., Wolf, D.E., 1985. Analysis of turbulent underexpanded jets, part II: shock noise features using SCIPVIS. AIAA J. 23, 669–677.

Shu, C.-W., Osher, S., 1988. Efficient implementation of essentially non-oscillatory shock-capturing schemes. J. Comput. Phys. 77, 439–471.

Shu, C.-W., Osher, S., 1989. Efficient implementation of essentially non-oscillatory shock-capturing schemes II. J. Comput. Phys. 83, 32–78.

Shu, C.-W., 1990. Numerical experiments on the accuracy of ENO and modified ENO schemes. J. Sci. Comput. 5, 127–150.

Shu, C.-W., Zang, T.A., Erlebacher, G., Whitaker, D., Osher, S., 1992. High-order ENO schemes applied to two- and three-dimensional compressible flow. Appl. Numer. Math. 9, 45–71.

Sinha, R., Zakky, V., Erdos, J., 1970. Flowfield analysis of plumes of two dimensional underexpanded jets by a time dependent method. AIAA J. 9, 2363–2370.

Tam, C.K.W., Jackson, J.A., Seiner, J.M., 1985. A multiple-scales model of the shock-cell structure of imperfectly expanded supersonic jets. J. Fluid Mech. 153, 123–149.

Tsai, Y.P., Christiansen, W.H., 1990. Two dimensional numerical simulation of shear layer optics. AIAA J. 28, 2092–2097.

Vatsa, V.N., Werle, M.J., Anderson, O.L., 1981. Solution of slightly underexpanded two-dimensional and axisymmetric co-flowing jets. AIAA J. 19, 303–310.

Winant, C.D., Browand, F.K., 1974. Vortex pairing: the mechanism of turbulent mixing-layer growth at moderate Reynolds number. J. Fluid Mech. 63, 237–255.

Xu, S., Aslam, T., Stewart, D.S., 1997. High resolution numerical simulation of ideal and non-ideal compressible reacting flows with embedded internal boundaries. Combust. Theory Model. 1, 113–142.

Zaman, K.B.M.Q., Reeder, M.F., Samimy, M., 1993. Control of an axisymmetric jet using vortex generators. Phys. Fluids 6, 778–793.